Supplementary Material: Self-similarity of spectral response functions for fractional quantum Hall states

CONTENTS

SI. HALDANE PSEUDOPOTENTIAL FORMALISM

In this section, we discuss the properties of FQH systems with interactions modeled using Haldane pseudopotentials. In Sec. SI A, we outline the derivation of Haldane pseudopotentials for the Coulomb and Yukawa interactions; in Sec. SI B, we benchmark the convergence of two-particle energy spectra; and in Sec. SI C, we analyze the effect on spectral response functions as we tune the interaction from lower- to higher-order pseudopotentials. Although the examples studied can be analyzed directly using exact diagonalization, we use a Haldane pseudopotential approach to contrast the effects of tuning the interaction range via the Yukawa mass, as shown in Sec. IV.A, and truncating two-body interactions with large relative angular momenta.

A. Derivation of the Haldane pseudopotentials

The derivation in this section is performed on a plane and in atomic units, where the Coulomb constant $k_e \equiv (4\pi\epsilon)^{-1} = 1$, the fermionic charge $q_f = 1$, and the magnetic length $l_B \equiv (2\pi N_\Phi)^{-1/2} = 1$.

The Haldane pseudopotentials[S1] in the n-th Landau level, $V_m^{(n)} \equiv \langle n, m|V|n, m\rangle$, may be written in momentum space as

$$V_m^{(n)} = \int \frac{\mathrm{d}\mathbf{q}}{2\pi} V(\mathbf{q}) \langle n, m|e^{\mathrm{i}\mathbf{q}\cdot\mathbf{r}}|n, m\rangle \,, \tag{S1}$$

where m is the pseudopotential index and $\mathbf{r}$, $\mathbf{q}$ are the position and momentum vectors, respectively.

Using the fact that the FQHE in the n-th Landau level with interaction potential $V(\mathbf{q})$ is equivalent to the FQHE in the 0-th Landau level with interaction potential $[L_n(q^2/2)]^2 V(\mathbf{q})$, coupled with the result $\langle m|e^{\mathrm{i}\mathbf{q}\cdot\mathbf{r}}|m\rangle = e^{-q^2} L_m(q^2)$, allows us to write

$$V_m^{(n)} = \int \frac{\mathrm{d}\mathbf{q}}{2\pi} V(\mathbf{q}) \left[L_n(q^2/2)\right]^2 L_m(q^2) e^{-q^2}, \tag{S2}$$

where L_n is the n-th Laguerre polynomial[S2,S3].

Finally, converting the momentum integral to polar coordinates yields

$$V_m^{(n)} = \int_0^\infty q\mathrm{d}q V(\mathbf{q}) \left[L_n(q^2/2)\right]^2 L_m(q^2) e^{-q^2}. \tag{S3}$$

1. Coulomb interaction

We use the explicit representation of a centrally-symmetric interaction $V(\mathbf{r}) = V(r)$ in momentum space,

$$V(q) = \int \frac{\mathrm{d}\mathbf{r}}{2\pi} V(r) e^{-\mathrm{i}\mathbf{q}\cdot\mathbf{r}}. \tag{S4}$$

Converting this momentum integral to polar coordinates, coupled with the fact that $e^{-\mathrm{i}\mathbf{q}\cdot\mathbf{r}} = \cos(\mathbf{q}\cdot\mathbf{r})$ since the interaction is a real and even function of r, allows us to write

$$V(q) = \int_0^\infty r\mathrm{d}r V(r) \int_0^{2\pi} \frac{\mathrm{d}\theta}{2\pi} \cos(qr\cos\theta). \tag{S5}$$

Furthermore, since the angular integral is a standard Bessel integral, this expression reduces to

$$V(q) = \int_0^\infty r\mathrm{d}r V(r) J_0(qr), \tag{S6}$$

where J_n is the n-th Bessel function of the first kind.

Specifically for the Coulomb interaction, $V^{\mathrm{C}}(r) = r^{-1}$, this yields

$$V^{\mathrm{C}}(q) = \int_0^\infty r\mathrm{d}r V^{\mathrm{C}}(r) J_0(qr) = \int_0^\infty \mathrm{d}r J_0(qr) = \frac{1}{q}. \tag{S7}$$

Inserting this result into the expression for the Haldane pseudopotentials, Eq. (S3), then yields

$$V_m^{C,(n)} = \int_0^\infty \mathrm{d}q \left[L_n(q^2/2)\right]^2 L_m(q^2) e^{-q^2}. \tag{S8}$$

Finally, in the LLL ($n = 0$), this integral can be evaluated analytically and written in closed form, such that

$$V_m^{C,(0)} = \frac{\sqrt{\pi}}{2}\, {}_2F_1(1/2, -m; 1; 1) = \frac{\sqrt{\pi}}{2} \frac{(2m-1)!!}{2^m m!}, \tag{S9}$$

where ${}_2F_1$ is the Gauss hypergeometric function. The asymptotic scaling as $m \to \infty$ is given as

$$V_m^{C,(0)} \sim \frac{2^{-5/4+\cos(2m\pi)/4} \pi^{\sin^2(m\pi)/2}}{\sqrt{m}}. \tag{S10}$$

2. Yukawa interaction

Similarly, using Eq. (S6), the Yukawa interaction, $V_\lambda^{\mathrm{Y}}(r) = r^{-1} e^{-\lambda r}$, may be written in momentum space as

$$V_\lambda^{\mathrm{Y}}(q) = \int_0^\infty r\mathrm{d}r V_\lambda^{\mathrm{Y}}(r) J_0(qr) = \frac{1}{\sqrt{\lambda^2 + q^2}}, \tag{S11}$$

where λ is the Yukawa scaling constant. Inserting this result into the expression for the Haldane pseudopotentials, Eq. (S3), yields

$$V_{\lambda,m}^{Y,(n)} = \int_0^\infty \mathrm{d}q \frac{q}{\sqrt{\lambda^2 + q^2}} \left[L_n(q^2/2)\right]^2 L_m(q^2) e^{-q^2}. \tag{S12}$$

In the LLL, this expression simplifies to

$$V_{\lambda,m}^{Y,(0)} = \frac{\lambda}{2\sqrt{\pi}} \Gamma(m + 1/2) U(m+1, 3/2, \lambda^2), \tag{S13}$$

where Γ is the gamma function and U is the confluent hypergeometric function of the second kind. The asymptotic scaling as $m \to \infty$ is given as

$$V_{\lambda,m}^{Y,(0)} \sim \frac{\lambda}{\sqrt{2}} e^{-m} m^m U(m+1, 3/2, \lambda^2). \tag{S14}$$

Plots of the Haldane pseudopotentials for both the Coulomb and Yukawa interactions are shown in Fig. S1.

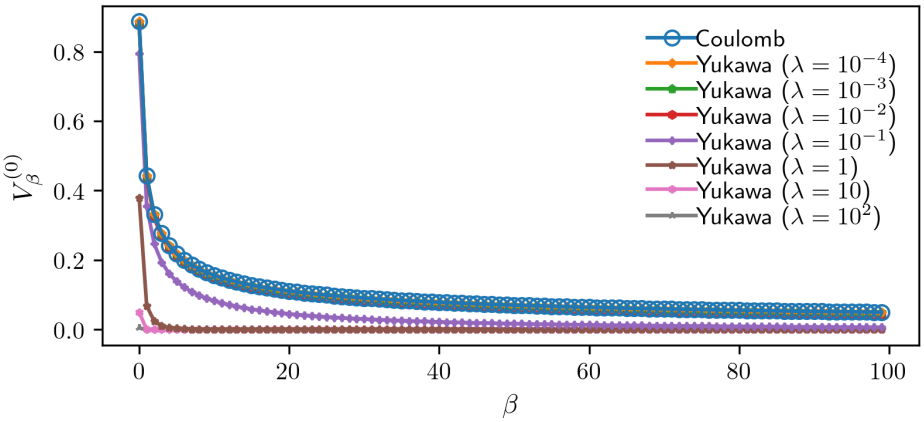

FIG. S1. **Haldane pseudopotentials.** Haldane pseudopotentials on a plane, in the LLL, for the Coulomb (S9) and Yukawa interactions (S13).

B. Convergence of two-particle energy spectra

One of the fundamental properties of Haldane pseudopotentials is their correspondence with the two-particle energy spectrum[S1]. On a sphere, it is straightforward to verify that the energy levels are completely equivalent to the Haldane pseudopotential coefficients. On a torus, however, the pseudopotential algebra is not exact and so different eigenstates can mix, as well as potentially be effected by boundary conditions. In light of this, we examine the convergence of the energy levels in a two-particle system relative to the pseudopotential coefficients.

We consider a system on a torus with two particles in the LLL, with a size defined by the number of flux quanta l. Subsequently, we compute the energy spectrum of this system for a particular Haldane pseudopotential coefficient corresponding to the Coulomb interaction V_i^{C}. For each coefficient V_i^{C}, the resulting energy spectrum consists of a set of three quasi-degenerate energies $\{E_i\}$ with all other energies equal to zero. The plots of $\bar{E}_i - V_i^{\mathrm{C}}$ as a function of l are shown in Fig. S2. In particular, here we define convergence when the relative error $|\bar{E}_i - V_i^{\mathrm{C}}|/V_i^{\mathrm{C}} < 1\%$ and we denote the first value of l where this occurs as l_{crit}.

From Fig. S2, we can gain several insights into the effectiveness of the Haldane pseudopotential representation on a torus. First and foremost, we can see that the higher-order Haldane pseudopotential coefficients are more difficult to reproduce than for lower orders, with the required system size l_{crit} scaling linearly with the order i. For example, although the first pseudopotential V_1^{C} is already reproduced at $l_{\mathrm{crit}} = 12$, the third pseudopotential V_5^{C} requires double this with $l_{\mathrm{crit}} = 24$, and so on. Second, we can conclude that for a given system with N_Φ flux quanta, the largest Haldane pseudopotential coefficient that should be employed in the interaction is $\beta \sim N_\Phi/2$. We note, however, that the precise value of this upper bound depends on system parameters, including the filling factor, and so cannot be precisely determined from Fig. S2. Physically, any coefficients larger than this threshold will be sensitive to the tails of the wave function wrapping around the cycles of the torus and so are severely effected by finite-size effects. Finally, we can see that at inadequate l not all of the energies are resolved, and so the quasi-degenerate set of $\{E_i\}$ contains at least one zero, which pulls the average down unpredictably. For larger system sizes, we observe the expected symmetric and monotonic convergence of the mean and standard deviation towards the Haldane pseudopotential coefficient in all cases.

Building on this, we consider the case of Haldane pseudopotentials modeling the Yukawa interaction. From Fig. S1, we can see that the form of the Yukawa pseudopotential drastically changes in the region $10^{-2} < \lambda < 1$. At $\lambda = 10^{-2}$, we observe a pseudopotential indistinguishable from the Coulomb pseudopotential on the scale of the plot, whereas at $\lambda = 1$ we observe a sharp cut-off, where only the first few pseudopotentials take significant non-zero values. Due to this sharp transition, it is no longer critical to consider higher-order pseudopotentials in order to accurately model the Yukawa interaction at large λ. Since the analysis in Fig. S2 is performed one pseudopotential at a time, the results are simply scaled for the Yukawa interaction. Hence, the relative error thresholds are unaffected and the scaling in Fig. S2(j) still holds. However, since the higher-order pseudopotentials are significantly smaller for the Yukawa interaction with large λ, the absolute error threshold $|\bar{E}_i - V_i| < 1\%$ is satisfied at drastically smaller system sizes.

In summary, although the Haldane pseudopotentials have a complete equivalence with their two-particle energy spectra on a sphere, this does not hold for the torus. On a torus geometry with N_Φ flux quanta, the Haldane pseudopotentials can only be used to model short-range interactions described by $\{V_1, V_3, \ldots, V_\beta\}$, where $\beta \ll N_\Phi$.

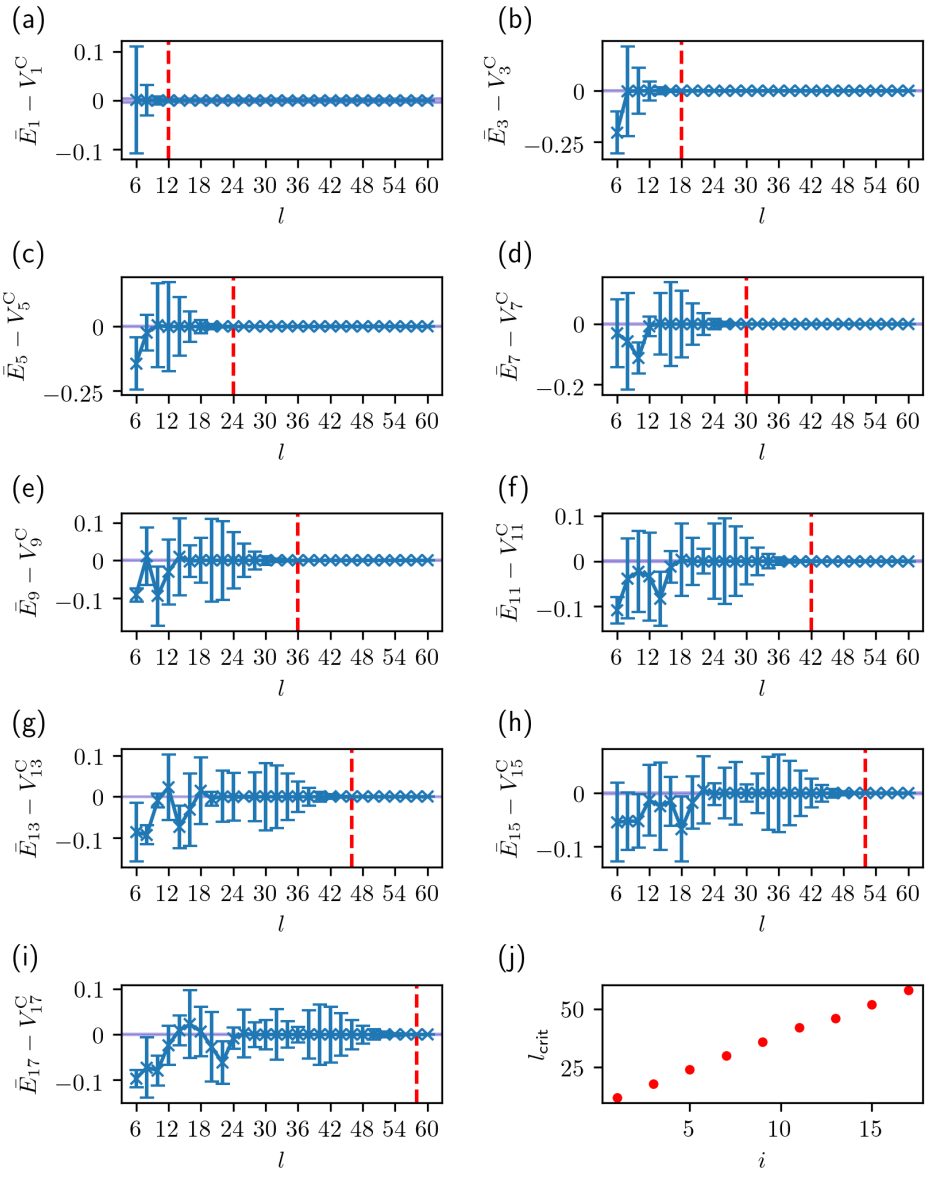

FIG. S2. **Convergence of two-particle energy spectra to Haldane pseudopotential coefficients.** (a–i) The set of quasi-degenerate energies $\{E_i\}$ corresponding to Coulomb pseudopotentials V_i^{C}, for the two-particle energy spectrum on a torus in the LLL, as a function of the number of flux quanta l. The mean $\bar{E}_i$ and standard deviation σ_i of $\{E_i\}$ are plotted and the $V_i^{\text{C}} \pm 0.01 V_i^{\text{C}}$ region is shaded blue. The first value of l for which $\bar{E}_i \pm \sigma_i$ is within 1% of V_i^{C} (l_{crit}) is marked with a red dashed line. (j) Scaling of l_{crit} as a function of Haldane pseudopotential coefficient i.

C. Tuning from lower- to higher-order Haldane pseudopotentials

To complement our analysis of the Coulomb and Yukawa interactions using an explicit diagonalization in Fourier space, we study the interactions using a Haldane pseudopotential description. The Haldane pseudopotential formalism is useful because most of the physics of interacting fermions in the LLL can be captured by its first few values, which greatly simplifies both analytical and computational complexity. Although originally applied to short-range interactions on the sphere, it has since been generalized to accommodate more diverse interactions on a range of geometries[S4]. Nevertheless, it is important to note that, unlike for the sphere, pseudopotential algebra is not exact on the torus and so a convergence of the energy spectrum will only be reached for the first few energy levels with short-range interactions relative to the system size.

In order to quantify the effectiveness of the first few Haldane pseudopotentials in capturing the physics of the

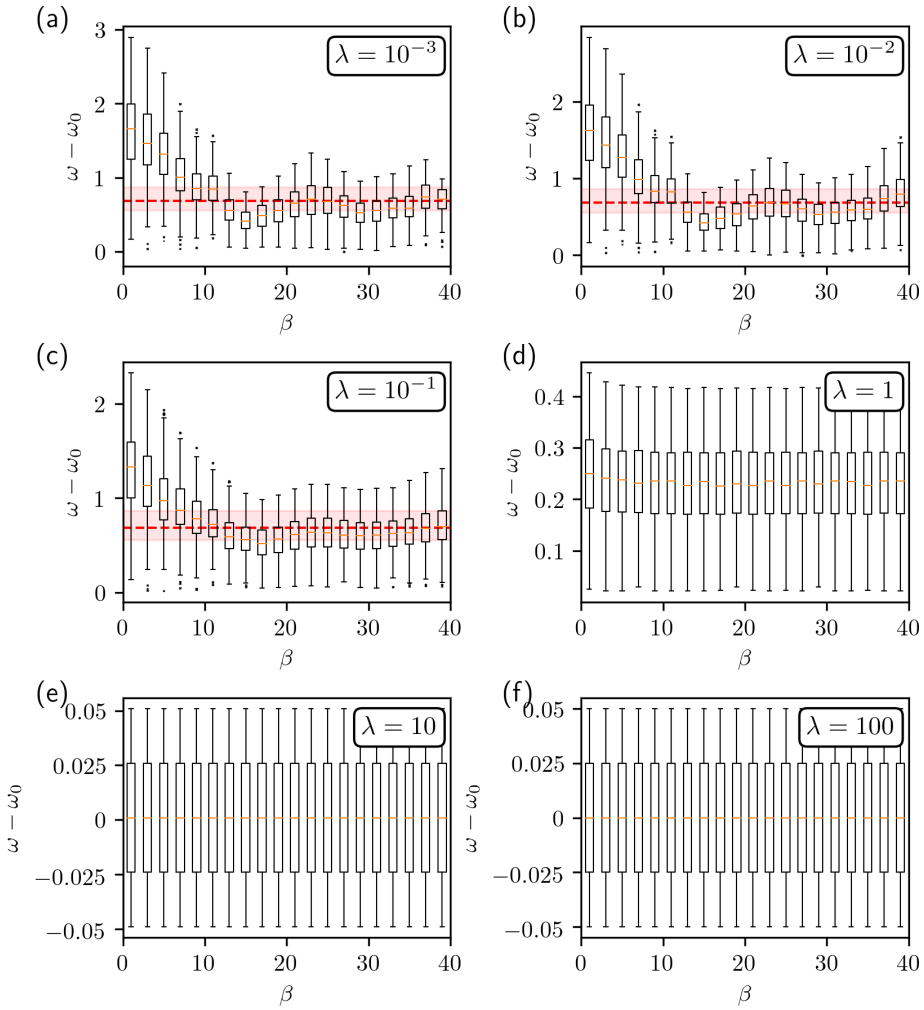

FIG. S3. **Convergence of the structure factor with Yukawa pseudopotential truncation.** Box plots showing the spread of the structure factor $I_{\bar{\rho}}(0,\omega)$ for the $\nu = 1/3$ FQH state on a torus, with $N_f = 6$ particles and $N_\Phi = 18$ flux quanta, stabilized by the LLL Haldane pseudopotentials corresponding to the Yukawa interaction $\{V_\lambda^{\mathrm{Y}}\} = \{V_{\lambda,0}^{\mathrm{Y}}, V_{\lambda,1}^{\mathrm{Y}}, \ldots, V_{\lambda,\beta}^{\mathrm{Y}}\}$, as a function of truncation parameter $\beta \in \{1, 3, \ldots, 39\}$ at a variety of λ. The median is labeled with an orange line, the interquartile range (IQR) is drawn with a box, and the whiskers extend to 1.5 times the IQR. All data points outside of this range are plotted as outliers. In (a–c) we additionally overlay the IQR and median for the exact Coulomb interaction from Fig. 1(b) in red. The computations were performed with a resolution of $\Delta\omega = 10^{-5}$, $\Delta I = 10^{-5}$, and $\epsilon = 10^{-4}$.

Laughlin state on the torus, we present the scaling of the structure factor as we increase the order of the pseudopotentials corresponding to the Yukawa interaction $\{V_\lambda^{\mathrm{Y}}\} = \{V_{\lambda,0}^{\mathrm{Y}}, V_{\lambda,1}^{\mathrm{Y}}, \ldots, V_{\lambda,\beta}^{\mathrm{Y}}\}$ in Fig. S3, where β is our truncation parameter. Although, it is physical to consider only small $\beta \ll N_\Phi$, since larger values may reflect eigenstate mixing and boundary conditions, we show an extended range of $\beta \in \{1, 3, \ldots, 39\}$ to additionally comment on numerical effects. In Fig. S3(a), we show the structure factor scaling in the Coulomb approximation $\lambda \approx 0$. From the plot, we can see that for $\beta \gtrsim N_\Phi/2$, we obtain a rough approximation of the structure factor corresponding to the Coulomb interaction. However, we note that for such a large number of pseudopotentials, the convergence of the energy levels is limited, which results in oscillations of the energy scale. These oscillations reflect the boundary interference arising from modeling large relative angular momenta on a finite torus. As we increase the value of λ, and hence decrease the interaction range, these boundary effects are gradually alleviated. Comparing Fig. S3(c) with Fig. S3(a), for example, we can see that the oscillations for $\beta \gtrsim N_\Phi/2$ are diminished and the approximation to the Coulomb interaction at $\beta \sim N_\Phi/2$ is improved. Further increasing the value of the Yukawa mass beyond $\lambda \sim 1$ exponentially decreases the range of the interaction and consequently, suppresses the domain of the structure factors. In the limit of $\lambda \to \infty$, the mean and standard deviation tend to zero, as we saw in Fig. 1(e). These results stress that Haldane pseudopotentials can work well on the torus *provided* a few compromises are reached. The number of pseudopotentials needs to be large

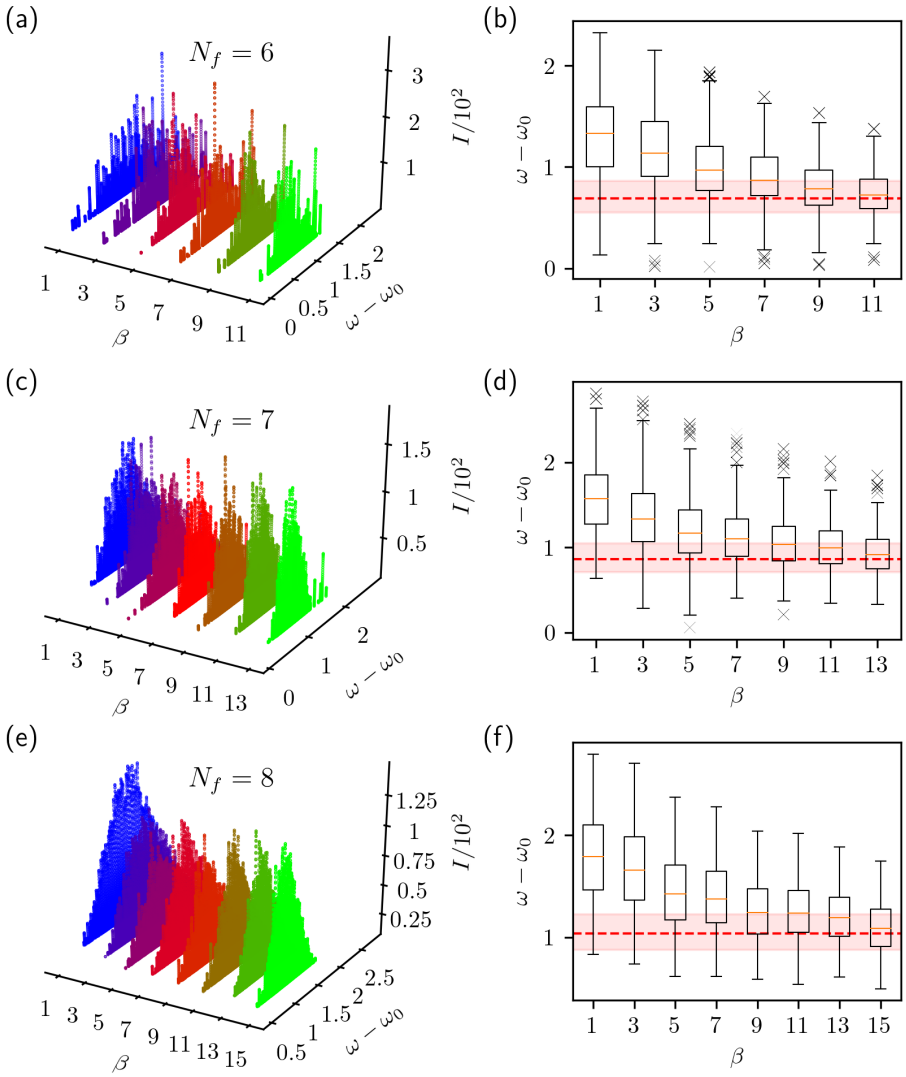

FIG. S4. **Approximating the Coulomb structure factor using Yukawa pseudopotentials at $\lambda = 0.1$.** Structure factor $I_{\bar{\rho}}(0, \omega)$ for the $\nu = 1/3$ FQH state on a torus, corresponding to the system in Fig. S3(c). (a,c,e) 3D plots showing the scaling of $I_{\bar{\rho}}(0, \omega)$ with truncation parameter $\beta \in \{1, 3, \ldots, \beta_{\max}\}$, where $\beta_{\max}$ is the smallest odd integer greater than $(N_\Phi + 2)/2$, for (a) $N_f = 6$, (c) $N_f = 7$, and (e) $N_f = 8$. (b,d,f) Box plots showing the spread of $I_{\bar{\rho}}(0, \omega)$ as a function of β, for (b) $N_f = 6$, (d) $N_f = 7$, and (f) $N_f = 8$. Outliers are shown explicitly as black crosses. The center and spread for the corresponding exact Coulomb distributions are overlaid in red. The computations were performed with a resolution of $\Delta\omega = 10^{-5}$, $\Delta I = 10^{-5}$, and $\epsilon = 10^{-4}$.

enough to accurately model the interaction potential, but not so large as to introduce boundary effects and eigenstate mixing. We find that, for this system, the optimal number of pseudopotentials is $\beta \sim N_\Phi/2$. Moreover, long-range interactions, such as the Coulomb interaction are more susceptible to finite-size effects. Therefore, the structure factor for these systems is most accurately modeled using Haldane pseudopotentials corresponding to weakly screened forms of the interaction.

Having shown that Haldane pseudopotentials can successfully model the Coulomb interaction provided the interaction is sufficiently screened, we now focus on the approximation obtained using the Yukawa interaction with $\lambda = 0.1$. In Fig. S4, we present a finite-size scaling of the structure factor from Fig. S3(c) for the particle numbers $N_f = 6, 7, 8$ and the physical values of the truncation parameter $\beta \ll N_\Phi$. From Fig. S4(a), we find a distribution with a single distinct mode akin to Fig. 1(b), with a comparable number of peaks and spread. Here, we observe the optimal approximation to the structure factor for the Coulomb interaction at $\beta = 11$, as shown in Fig. S4(b). As we increase the particle number in Figs. S4(c–f), the number of pseudopotentials required for an accurate approximation also

increases, such that optimal number is consistently $\sim N_\Phi/2$. This is the threshold that maximizes the accuracy of the interaction potential before boundary effects from the finite torus manifest, however we note that the precise value is dependent on system parameters, such as the filling factor. In addition to this, there are a few notable trends as we increase the system size. First, as was suggested by the results in Fig. 2, we find that the peak fluctuations are suppressed with increasing system size, where we no longer observe any outliers in the box plots in Fig. S4(f), compared to Figs. S4(b,d), for example. Second, we observe that for a restricted set of pseudopotentials, the approximation is more accurate for smaller system sizes. For example, the $\beta = 1$ approximation for $N_f = 6$ is more accurate, in relative terms, than the $\beta = 1$ approximation for $N_f = 8$. Finally, we can see that by comparing Fig. S4(a) and Fig. 1(b), for instance, the features near the bulk of the response spectra are reproduced more rapidly than the structure at the edges. These points notwithstanding, the structure factors presented here are a fair approximation of that for the long-range Coulomb potential in Fig. 1(b) and come at a significantly reduced numerical cost.

SII. DETAILS OF THE LANCZOS ALGORITHM

The underlying motivation behind the Lanczos algorithm is to compute the eigendecomposition of a Hermitian Hamiltonian H by variationally minimizing the energy functional $E[\Psi] = \langle\Psi|H|\Psi\rangle / \langle\Psi|\Psi\rangle$. Progress is made towards this goal by using an iterative procedure that subsequently explores the relevant parts of the Hilbert space.

In its most basic form, the Lanczos algorithm takes a normalized input vector $|v_0\rangle = |\Psi\rangle / \sqrt{\langle\Psi|\Psi\rangle}$, orthonormalizes $H|v_0\rangle$ with respect to $|v_0\rangle$ to obtain $|v_1\rangle$, and then finds the variational state of lowest energy by diagonalizing H in the two-dimensional subspace $\mathrm{span}(|v_0\rangle, |v_1\rangle)$. This variational state of lowest energy is then used as the input for the next minimization step, and so on, until the desired eigenenergy converges.

Building on this idea, efficient implementations directly perform $M-1$ such iterations by finding the variational state of lowest energy in the M-dimensional Krylov space $\mathcal{K}^{M-1}(|v_0\rangle) = \mathrm{span}(|v_0\rangle, H|v_0\rangle, H^2|v_0\rangle, \ldots, H^{M-1}|v_0\rangle)$, where $\{|v\rangle\}$ is the set of Lanczos vectors. As before, the algorithm starts with a normalized input vector $|v_0\rangle$. It then orthogonalizes $H|v_0\rangle$ with respect to $|v_0\rangle$ and normalizes to yield $|v_1\rangle = |\tilde{v}_1\rangle / \sqrt{\langle\tilde{v}_1|\tilde{v}_1\rangle}$, where $|\tilde{v}_1\rangle = (1 - |v_0\rangle\langle v_0|)H|v_0\rangle$. Similarly, $|\tilde{v}_2\rangle$ is constructed by orthogonalizing $H|v_1\rangle$ with respect to the two previous Lanczos vectors, such that $|\tilde{v}_2\rangle = H|v_1\rangle - a_1|v_1\rangle - b_1|v_0\rangle$, where $a_n = \langle v_n|H|v_n\rangle$ and $b_n = \langle v_{n-1}|H|v_n\rangle$. From the second step onwards, the iteration proceeds in the same manner, by orthonormalizing $H|v_n\rangle$ with respect to $|v_n\rangle$ and $|v_{n-1}\rangle$, i.e. using $|\tilde{v}_{n+1}\rangle = H|v_n\rangle - a_n|v_n\rangle - b_n|v_{n-1}\rangle$ followed by $|v_n\rangle = |\tilde{v}_n\rangle / \sqrt{\langle\tilde{v}_n|\tilde{v}_n\rangle}$. Crucially, due to the Hermiticity of the Hamiltonian H, as well as the orthogonality of the Lanczos vectors $\{|v\rangle\}$, the resulting basis is orthogonal (to within numerical precision) and only the current and immediately preceeding Lanczos vectors are needed to compute the subsequent vector. This means that the Hamiltonian may be expressed as

$$H|v_n\rangle = b_n|v_{n-1}\rangle + a_n|v_n\rangle + b_{n+1}|v_{n+1}\rangle . \tag{S15}$$

Therefore, in matrix form, the original $N \times N$ Hermitian Hamiltonian matrix H can be represented approximately by a $M \times M$ tridiagonal real symmetric Lanczos Hamiltonian matrix $\check{H}$ in Krylov space, given as

$$\check{H} = \begin{pmatrix} a_0 & b_1 & & & \\ b_1 & a_1 & b_2 & & \\ & b_2 & a_2 & \ddots & \\ & & \ddots & \ddots & b_{M-1} \\ & & & b_{M-1} & a_{M-1} \end{pmatrix}, \tag{S16}$$

where $M \leq N$.

Although the Lanczos algorithm does not compute the eigendecomposition of H, it takes a significant step towards this goal, by yielding a tridiagonal matrix $\check{H}$ that can be readily diagonalized. Moreover, since the Lanczos algorithm is an iterative method, useful results can be obtained without the algorithm running to completion. Most pertinently, extremal eigenvalues of $\check{H}$ show good agreement with those of the original system, even when the number of Lanczos iterations is much smaller than the dimension of the original Hamiltonian, $M \ll N$[S5–S7].

SIII. DERIVATION OF THE MOMENTUM-AVERAGED DENSITY OPERATOR ON A TORUS

Consider a free charged fermion in the xy-plane in the presence of a perpendicular magnetic field $\mathbf{B} = B\hat{\mathbf{z}}$. The fermion motion is typically parameterized using its center-of-mass coordinates (X, Y) and characterized by the magnetic length l_B. In Landau gauge with a conserved y-momentum, k_y, it can be shown that the single-particle ground

states may be written as

$$\phi(x,y) \sim e^{\mathrm{i}k_y y} \exp\left(-(X-x)^2/2l_B^2\right), \tag{S17}$$

where $X = -k_y l_B^2$. This shows that the wavefunctions are localized in the x-direction but extended in y.

When the fermion is confined to a rectangular sample of sides L_x by L_y, then the degeneracy of the LLL is determined by the number of allowed k_y such that $0 \leq X < L_x$. Applying periodic boundary conditions to Eq. (S17), we obtain $k_y = X_j/l_B^2 = 2\pi j/L_y$, where $j = 0, \ldots, N_\Phi - 1$ is an integer bounded by the degeneracy of the LLL, $N_\Phi = L_x L_y/2\pi l_B^2$. There are consequently N_Φ LLL eigenstates, which may be written as

$$\phi_j(x,y) \sim \sum_{m=-\infty}^{\infty} e^{\mathrm{i}(X_j + mL_x)y/l_B^2} \exp\left(-(X_j + mL_x - x)^2/2l_B^2\right), \tag{S18}$$

where $0 \leq j < N_\Phi$. The degeneracy is equivalent to the total number of flux quanta, such that $N_\Phi \equiv \Phi/\Phi_0$, where Φ is the magnetic flux and Φ_0 is the flux quantum. From now on, we set the magnetic length to one $l_B = 1$.

In order to compute the density operator on the torus we expand in the basis of LLL orbitals, such that

$$\rho_{\mathbf{q}} = \sum_{j,j'} \hat{\rho}_{j,j'}(\mathbf{q}) c_j^\dagger c_{j'}, \tag{S19}$$

where $c_j^{(\dagger)}$ are the annihilation (creation) operators for the Landau level orbitals ϕ_j (S18) and $\hat{\rho}_{j,j'}(\mathbf{q})$ is the Fourier transform of the normalized particle density coefficients, or form factor, defined as

$$\hat{\rho}_{j,j'}(\mathbf{q}) \equiv \int \mathrm{d}\mathbf{r}\, e^{\mathrm{i}\mathbf{q}\cdot\mathbf{r}} \hat{\phi}_j(\mathbf{r}) \hat{\phi}_{j'}^*(\mathbf{r}), \tag{S20}$$

$\mathbf{r} \equiv (x,y)$ and $\mathbf{q} \equiv (q_x, q_y)$ are position and momentum conjugate variables, and the hats denote normalization.

Starting with the form factor, we compute the Fourier transform of

$$\hat{\rho}_{j,j'}(x,y) = \frac{\phi_j(x,y)\phi_{j'}^*(x,y)}{N_f}, \tag{S21}$$

where N_f is a normalization constant, corresponding to the total particle number.

Computing the denominator of Eq. (S21), the total particle number

$$N_f = \sum_j \int_0^{L_x} \mathrm{d}x \int_0^{L_y} \mathrm{d}y\, \phi_j^*(x,y)\phi_j(x,y), \tag{S22}$$

yields, in terms of the number of repetitions of the simulation cell in the x- and y-directions, N_x, N_y,

$$N_f = \frac{1}{N_x N_y} \sum_j \int \mathrm{d}x\mathrm{d}y\, \phi_j^*(x,y)\phi_j(x,y). \tag{S23}$$

Working with large N_x, N_y allows us to extend the integration range. Performing the y-integral yields

$$N_f = \frac{2\pi L_y}{N_x L_x} \sum_{m=-\infty}^{\infty} \int \mathrm{d}x \exp\left(-\frac{1}{2}x^2 - \frac{1}{2}(x - mL_x)^2\right), \tag{S24}$$

where we have invoked the momentum periodicity in the y-direction. Subsequently, performing the x-integral yields

$$N_f = 2\pi\sqrt{\pi} L_y \sum_{m=-\infty}^{\infty} \exp\left(-m^2 L_x^2/4\right). \tag{S25}$$

In a similar fashion, we can compute the Fourier transform of the numerator of Eq. (S21), the unnormalized particle density coefficients

$$\rho_{j,j'}(\mathbf{q}) = \frac{1}{N_x N_y} \int \mathrm{d}\mathbf{r}\, e^{i\mathbf{q}\cdot\mathbf{r}} \phi_j(\mathbf{r}) \phi_{j'}^*(\mathbf{r}). \tag{S26}$$

As before, working with large N_x, N_y allows us to extend the integration range, and we can ultimately take $N_i \to \infty$ to obtain complete Gaussian integrals along x. Performing the y-integral yields

$$\rho_{j,j'}(\mathbf{q}) = \frac{2\pi L_y}{N_x L_x}\delta(X_j - X'_j + q_y) \sum_{m=-\infty}^{\infty} \int \mathrm{d}x\, e^{\mathrm{i}q_x x} \exp\left(-\frac{1}{2}(x - X'_j)^2 - \frac{1}{2}(x - X_j - mL_x)^2\right), \tag{S27}$$

where we have again employed the momentum periodicity in the y-direction. Finally, evaluating the integral along x yields

$$\rho_{j,j'}(\mathbf{q}) = 2\pi\sqrt{\pi} L_y \delta(X_j - X'_j + q_y) \sum_{m=-\infty}^{\infty} \exp[\chi_{j,j',m}(q_x)], \tag{S28}$$

where

$$\chi_{j,j',m}(q_x) \equiv \left(\frac{X'_j + X_j + mL_x + \mathrm{i}q_x}{2}\right)^2 - \frac{(X_j + mL_x)^2}{2} - \frac{X'^2_j}{2}, \tag{S29}$$

and hence the form factor is given as

$$\hat{\rho}_{j,j'}(\mathbf{q}) = \delta(X_j - X'_j + q_y) \frac{\sum_{m=-\infty}^{\infty} \exp \chi_{j,j',m}(q_x)}{\sum_{m=-\infty}^{\infty} \exp\left(-m^2 L_x^2/4\right)}. \tag{S30}$$

By invoking the q_x periodicity of the form factor, we can integrate out the q_x dependence by summing over momentum modes on the torus. This leaves us with an expression for the density operator that is only dependent on the q_y modes, which has analogous properties to the conserved k_y momentum in Landau gauge. Hence, using these coefficients in the general expansion of the density operator (S19), we arrive at our final expression for the q_x-momentum-averaged density operator used in the main text

$$\bar{\rho}_{q_y} = \sum_{m=0}^{N_\Phi - 1} \rho_{q_x = \frac{2\pi m}{L_x}, q_y}. \tag{S31}$$

[S1] F. D. M. Haldane, Phys. Rev. Lett. **51**, 605 (1983).
[S2] A. H. MacDonald, "Introduction to the physics of the quantum Hall regime," (1994), arXiv:9410047 [cond-mat.str-el].
[S3] J. K. Jain, *Composite Fermions* (Cambridge University Press, 2007).
[S4] K. Pakrouski, *Fractional quantum Hall e ect and quantum spin Hall e ect in semiconductor heterostructures*, Ph.D. thesis, ETH Zurich (2017).
[S5] Z. Bai, J. Demmel, J. Dongarra, A. Ruhe, and H. van der Vorst, *Templates for the Solution of Algebraic Eigenvalue Problems*, edited by Z. Bai, J. Demmel, J. Dongarra, A. Ruhe, and H. van der Vorst (Society for Industrial and Applied Mathematics, 2000).
[S6] E. Koch, "The Lanczos Method," in *The LDA+DMFT approach to strongly correlated materials*, Schriften des Forschungszentrums Jülich. Reihe modeling and simulation, Vol. 1, edited by E. Pavarini, E. Koch, A. Lichtenstein, and D. Vollhardt (Forschungszenrum Jülich GmbH Zentralbibliothek, Verlag, Jülich, 2011) Chap. 8, p. getr. Zählung, record converted from VDB: 12.11.2012.
[S7] P. E. Dargel, A. Wöllert, A. Honecker, I. P. McCulloch, U. Schollwöck, and T. Pruschke, Phys. Rev. B **85**, 205119 (2012).